

Depth Calibration of Double-sided Strip Germanium Detectors for the Compton Spectrometer and Imager Satellite

Field R. Rogers^{a,*}, Sean N. Pike^b, Samer Alnussirat^a, Robin Anthony-Petersen^a, Steven E. Boggs^b, Felix Hagemann^a, Sophia E. Haight^b, Alyson Joens^a, Carolyn Kierans^c, Alexander Lowell^a, Brent Mochizuki^a, Albert Y. Shih^c, Clio Sleator^d, John A. Tomsick^a, Andreas Zoglauer^a

^a*Space Sciences Laboratory, University of California, Berkeley, 7 Gauss Way, Berkeley, CA 94720, USA.*

^b*Department of Astronomy & Astrophysics, University of California, San Diego, 9500 Gilman Drive, La Jolla, CA, 92093, USA.*

^c*NASA Goddard Space Flight Center, 8800 Greenbelt Road, Greenbelt, MD, 20771, USA.*

^d*U.S. Naval Research Laboratory, 4555 Overlook Ave., SW, Washington, DC, 20375, USA.*

Abstract

Double-sided strip high-purity germanium detectors with three-dimensional position reconstruction capability have been developed over three decades, with space-based applications in high-energy astrophysics and heliophysics. Position resolution in three dimensions is key to reconstruction of Compton scattering events, including for the upcoming Compton Spectrometer and Imager (COSI) satellite mission. Two-dimensional position reconstruction is enabled by segmentation of the two detector faces into orthogonal strip contacts, enabling a pixelized analysis. The depth of an interaction cannot be measured directly but must be inferred from the charge collection time difference between the two faces of the detector. Here, we demonstrate for the first time the depth calibration of a detector with the COSI satellite geometry read out using an application specific integrated circuit (ASIC) developed for the COSI mission. In this work, we map collection time difference to depth using the Julia-based simulation package `SolidStateDetectors.jl` and validate it with comparison to the timing distributions observed in data. We also use simulations and data to demonstrate the depth resolution on a per-pixel basis, with $> 90\%$ of pixels having < 0.9 mm (FWHM) resolution at 59.5 keV and < 0.6 mm (FWHM) resolution at 122.1 keV.

Keywords: Position Reconstruction, Solid State Detectors, Germanium Sensors, Gamma-ray Instrumentation, Satellite Instrumentation, COSI

1. Introduction

Technology for double-sided strip high-purity germanium detectors (GeDs) has been developed over multiple decades [1, 2, 3, 4, 5, 6, 7, 8, 9, 10]. These sensors combine the excellent energy resolution capability characteristic of germanium with three-dimensional position resolution capability enabled by their geometry. Additionally, they are well-suited for γ -ray detection because the electron density of germanium facilitates a relatively high Compton scattering probability and containment of γ -rays within a compact instrument. The usefulness of such GeDs for diverse scientific programs and their suitability for high-altitude and space environments has been demonstrated by their successful operation aboard the Gamma-Ray Imager/Polarimeter for Solar flares (GRIPS) [11], Nuclear Compton Telescope (NCT) [12, 13], and Compton Spectrometer and Imager (COSI) [14] stratospheric balloons.

The COSI satellite [15, 16, 17] is an upcoming compact Compton telescope that will survey the 0.2 – 5 MeV sky

as a NASA Small Explorer mission. Despite a rich scientific potential, MeV-scale astrophysics has thus far been underexplored compared to other energy bands due to the experimental challenges of operating in the Compton scattering regime – including the need for a high-altitude or space-based mission, high instrumental and astrophysical backgrounds, and low interaction cross sections. COSI’s 16 GeDs enable the energy and position resolution necessary for reconstruction of Compton scattering events. They thus facilitate sensitivity for MeV astrophysics, especially narrow lines, despite the challenges. The energy and position resolution of the GeDs directly impact COSI’s angular resolution, critical for imaging capability and background suppression [18].

Each COSI satellite GeD (pictured in Fig. 1) features a ~ 15 mm-thick planar geometry. Each face is segmented into 64 strip contacts (1.162 mm strip pitch), with the strips on the low voltage (LV; cathode) face orthogonal to those on the positive high voltage (HV; anode) face. Defining the intersection of a unique HV and LV strip pair as a 1.162×1.162 mm² pixel for analysis purposes enables direct 2D position reconstruction as well as a pixelized calibration.

*Corresponding author

Email address: fieldr@berkeley.edu (Field R. Rogers)

At the energies considered in this work, an incident γ -ray typically interacts either via Compton scattering or photoabsorption. In the case of Compton scattering, it may scatter one or more times prior to either photoabsorption in or escape from the GeD. At each interaction site, ~ 340 electron-hole pairs are generated per keV, resulting in a cloud of free charge carriers. The electron cloud and hole cloud propagate toward opposite faces of GeD at typical velocities of a few 10^6 cm/s, depending on the temperature, electric field strength, and material properties. As they propagate, the charge clouds also expand due to Coulomb repulsion and diffusion.

The motion of the charges induces a signal on the contacts. A weighting potential [19] is defined to describe the signal induced on a particular contact by charge movement at some position. The COSI GeDs are subject to the small-pixel effect [20], where the signals on small contacts are dominated by charge cloud motion close to the contacts. Thus, the signal on any HV (LV) contact is predominantly induced by the motion of electrons (holes) as they approach that contact. Effects including electronic and environmental noise, charge trapping in the bulk, charge sharing between strips, signal loss to the gaps between strips, capacitive cross talk, and transient signals all contribute to the GeD response [21, 22, 23, 24, 25, 26, 27].

The depth (z) of an interaction cannot be measured directly. Instead, z must be inferred from the charge collection time difference (τ_{CTD}), defined as the time elapsed between the signal on the HV contact and the signal on the LV contact. The $\tau_{\text{CTD}}-z$ relation depends on factors including operating bias voltage, impurity concentration, detector thickness, and temperature-dependent charge carrier mobility in the material. The small pixel effect means that the weighting potential depends strongly on z near the faces of the GeD, so the relation is nonlinear¹. Thus, the $\tau_{\text{CTD}}-z$ mapping must be calculated or simulated for each GeD at its operating temperature and bias voltage.

For calibration purposes, it is possible to either a) place a flood source at a known position, model the distribution of interaction depths relative to the source position, and compare the data to the model or b) use a collimated source or fan beam to illuminate some of the edge pixels at a known depth. This work utilizes a flood source at a known position. The distribution of energy depositions as a function of z can be calculated analytically or simulated using a particle simulation toolkit such as **Geant4** [28], where the latter method can more easily incorporate the effects of scattering in passive materials.

Depth calibration for similar GeDs has previously been demonstrated [2, 3, 4, 6, 21, 18]. Here, we present the first depth calibration of a GeD with the COSI satellite geometry with 1.162 mm strip pitch, and the first using the COSI satellite-model readout electronics. We also demonstrate

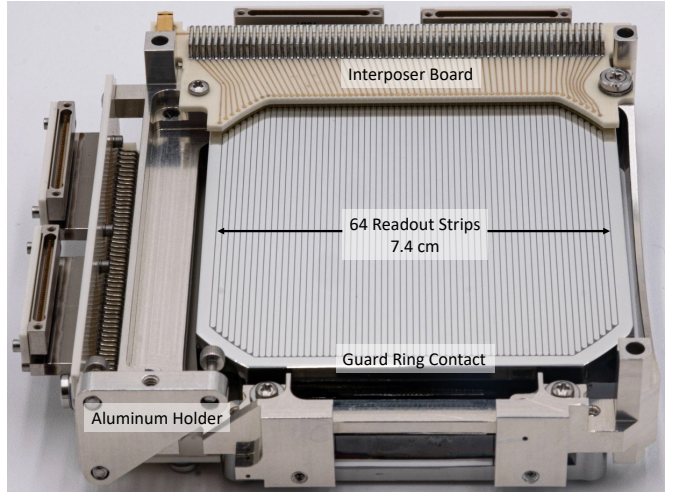


Figure 1: A 64-strip GeD in an engineering-model aluminum holder. The interposer board and connectors at the top of the image carry signal from the 64 HV strip contacts (visible and oriented vertically in this image), while the connectors on the left carry signal from the 64 LV strip contacts (hidden, and oriented horizontally). The guard ring contact encloses the 64 strip contacts on each face.

the use of the Julia-based [29] **SolidStateDetectors.jl**² [30] framework to simulate the timing response of these double-sided strip GeDs. Sec. 2 presents the experimental setup including modeling of z distributions and the preparation of the calibration data. Sec. 3 details the simulations of electric field and weighting potentials, charge cloud transport within the GeD, the readout electronics, leading to a $\tau_{\text{CTD}}-z$ mapping and a model τ_{CTD} distribution. In Sec. 4, we fit the data with the model to obtain the $\tau_{\text{CTD}}-z$ mapping and the depth resolution for a single pixel, and in Sec. 5, we discuss the results from fitting data from all of the pixels individually.

2. Data Collection

2.1. Detector, Readout, and Operation

This work demonstrates the depth calibration of a single COSI satellite engineering-model GeD, HP52301-1, with its readout electronics. HP52301-1 was fabricated at Lawrence Berkeley National Laboratory using amorphous Si and Ge contact technology [7, 8, 10]. Its physical characteristics are summarized in Tab. 1. As illustrated in Fig. 1, each COSI satellite GeD is a ~ 15 mm-thick crystal cut from a 10 cm-diameter boule. The instrumented area is the intersection of an ~ 8 cm square with this circular geometry. The 7.44 cm-wide fiducial area is segmented into 64 readout strips on the LV face and 64 orthogonal strips on the HV face. A guard ring contact encloses the strips on each side of the detector, improving the noise performance by mitigating surface leakage current to

¹ Additionally, for events close to the HV (LV) face, the holes (electrons) also contribute to the signal, resulting in a steep slope near the faces.

²<https://github.com/JuliaPhysics/SolidStateDetectors.jl>

the strips. The geometry is distinct from previous GeD models in strip number and pitch.

The operational setup, in which a single GeD is held within a custom liquid-nitrogen-cooled vacuum cryostat, is based on that in Ref. [10]. The temperature of the GeD is ~ 83 K, extrapolated based on a sensor located on a metal bracket holding the detector holder assembly within the cryostat. HP52301-1 was operated under an external 1000 V bias, compared to the depletion voltage $V_D \sim 175$ V.

Each GeD is read out by six 32-channel custom application-specific integrated circuit (ASIC) chips [31], which provide energy and timing information for each strip within the power, volume, and data bandwidth constraints of a space mission. All six ASICs are controlled by a single field-programmable gate array (FPGA) and respect its clock. The strips are read out by four ASICs, two AC-coupled to the HV strips, and two DC-coupled to the LV strips. The LV and HV guard ring contacts are read out by one channel each of the final two ASICs. In each ASIC channel, the signal is first processed by a preamplifier circuit with an 8.33 MHz low-pass order-2 Butterworth filter. Then, the preamplifier output is processed by two different shaping circuits. The ‘slow shaper’, an order-5 Gaussian filter with peaking time set to 2 μ s, is used for the energy scale, where the analog-digital converter (ADC) records the peak amplitude of the slow shaper output. Meanwhile, the ‘fast shaper,’ an order-3 Gaussian filter with peaking time set at 60 ns, is used to calculate the timing of charges arriving at the strip. When the fast shaper peaks, the ASIC begins to ramp an analog voltage for that readout channel. The time-amplitude conversion (TAC) is the digitized value of the voltage at the end of the readout window for an event. A ‘slow threshold’ (typically ~ 10 keV) and a ‘fast threshold’ (typically ~ 35 keV) are independently set for the slow and fast shaper on each channel.

All six ASICs are triggered when any readout channel exceeds its slow threshold. ADC and TAC values are then recorded for each ASIC channel exceeding its slow threshold within a fixed window and for all adjacent strips. For each channel, flags indicate if the slow and fast thresholds were exceeded. If the fast threshold is not exceeded for a channel, then the fast shaper does not trigger a voltage ramp, and instead the ASIC begins to ramp the voltage at the peak of the slow shaper, resulting in a smaller TAC value. Each energy deposition results in charge on both the HV and LV faces, such that the resulting data typically consists of at least one channel over threshold on either face of the GeD.

2.2. Datasets and Event Selection

This section outlines the depth calibration datasets, energy and timing calibration, and the event selection leading to the generation of τ_{CTD} distributions from data.

The data used in the depth calibration were obtained using ^{241}Am and ^{57}Co sources placed outside of the cryo-

Table 1: The physical characteristics and operation conditions of GeD HP52301-1.

Number of strips per side	64
Strip contact width	1.0166 mm
Strip gap width	0.1452 mm
Guard ring width	2.5 mm*
Crystal lateral dimension	79.5 mm
Crystal thickness	15.2 mm
Contact thickness	0.5 μ m
Impurity type	p-type
Impurity concentration	$1.3 \cdot 10^9 \text{ cm}^{-3}$
Estimated depletion voltage, V_D	175 V
Operating bias voltage	1000 V
Operating temperature	83 K
Crystal Orientation in \hat{z}	$\langle 001 \rangle$

*The guard ring contact width varies around the GeD perimeter as determined by the precise positioning of the photolithography mask used to apply the strips.

stat, at a distance roughly 20 cm from either the HV or the LV face of the GeD and roughly centered with respect to the face. Photons interacting in matter are characterized by an energy-dependent attenuation coefficient λ , such that the intensity $I(r)$ of a photon beam that has traveled distance r in a material is given by

$$I(r) = I(0) \cdot e^{-r/\lambda}. \quad (1)$$

The number of photoabsorption events in the range $(r, r + \delta r)$ is proportional to $I(r)$. For each source, Tab. 2 lists the attenuation coefficients for γ -rays at the line energies of interest in this calibration.

For the pixelated GeD geometry with a source placed at a distance from the center of the HV or LV face, the effective $I(z)$ in a pixel is modified relative to Eq. (1), due to a) the angular dependence of the coherent scattering cross section, b) the angle between \hat{r} and \hat{z} for off-center pixels, c) the z -dependence of the solid angle subtended by a pixel. **Geant4** simulations demonstrated that for the source positioned at ~ 20 cm, $I(z)$ in a given pixel still follows an approximately exponential distribution in depth, with an effective attenuation depth in a central pixel of $\lambda_z^c \sim 0.98\lambda$ (0.90λ) at 59.5 keV (122.1 keV). Depending on their exact position, the effective attenuation depth λ_z for non-central pixels differs from λ_z at the percent level.

The energy and TAC calibrations were generated and applied on a per-strip basis. The energy calibration was generated for each strip of HP52301-1 using **Melinator** photopeak-fitting software³ [33] and dedicated datasets recorded with ^{241}Am , ^{57}Co , and ^{137}Cs calibration sources following the procedure detailed in previous work [9, 22].

³**Melinator** is packaged with the Medium-Energy Gamma-ray Astronomy library (**MEGAlib**), available online at <https://github.com/zoglauer/megplib>.

Table 2: The radioisotopes and selected line energies used in the depth calibration. The mass attenuation coefficients (λ/ρ) are from the NIST XCOM database [32], neglecting coherent scattering. The attenuation coefficients in mm (λ) are calculated using the Ge density of $\rho = 5.323 \text{ g/cm}^3$. λ_z^c is the effective attenuation depth in a central pixel based on **Geant4** simulations.

Isotope	Energy [keV]	λ/ρ [$\text{cm}^2 \text{g}^{-1}$]	λ [mm]	λ_z^c [mm]
^{241}Am	59.5	1.945	0.97	0.95
^{57}Co	122.1	0.327	5.75	5.20

Meanwhile, the TAC calibration was calculated for each strip by injecting 50 mV pulses (corresponding to $\sim 50 \text{ keV}$ signals) at known times after a trigger, to obtain a linear conversion from raw clock values to nanoseconds.

Low-level cuts were imposed on the strip-hits to ensure data quality. Strip-hits that did not exceed the slow thresholds were not considered in this analysis. Requirements were then placed on the timing for each strip-hit within an event. A software coincidence window of 600 ns, much longer than the observed $\sim 200 \text{ ns}$ maximum charge drift time for HP52301-1, was imposed based on TAC values. Additionally, to remove chance coincident events, strip-hits were required to have TAC values corresponding to the window when the ASICs were accepting events rather than reading out data.

Event selection criteria were applied to obtain a clean sample of single-site events with a well-defined energy:

- 1. Energy threshold:** An 8 keV (17 keV) software energy threshold was imposed on the strip-hits in the ^{241}Am (^{57}Co) data to mitigate impacts of strip-to-strip threshold variation in the subsequent selection⁴.
- 2. Single-pixel events:** Events were selected with exactly two strip-hits above the energy threshold, one strip-hit on either face.
- 3. Line energy:** To select a clean sample of photo-peak events, events were selected for which one of the two strip-hits fell within $\pm 3.5 \text{ keV}$ of the line energy (i.e., within $\sim 3\sigma$ of the line centroid considering the energy resolution on a typical strip). The other strip was required to be less than the line energy $+ 3.5 \text{ keV}$. This relatively permissive selection allows events with sub-threshold charge sharing or trapping on one side of the detector to be included in the analysis, mitigating systematic depth-dependent effects in the event selection.
- 4. Fast timing:** Events were rejected if either of the constituent strip-hits did not exceed its fast threshold and thus lacked a valid fast-shaper TAC value.

⁴The software threshold is $\sim 14\%$ of the line energy in both cases, which allows some charge to be shared onto adjacent strips. Because there is more charge sharing at higher energies and the degree of charge sharing depends on the interaction depth, this choice also mitigates depth-dependent selection effects when requiring exactly one strip-hit per face.

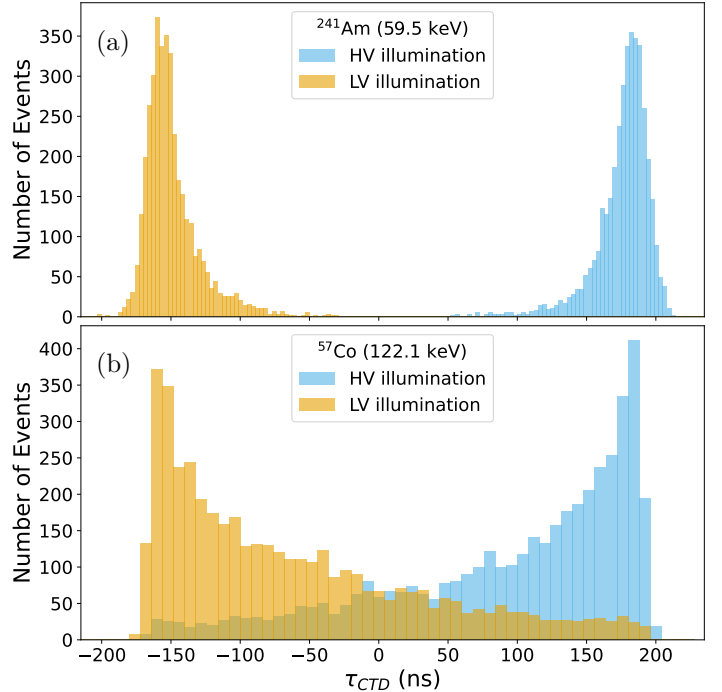


Figure 2: τ_{CTD} distributions for an example pixel in HP52301-1 are shown for events in the 59.5 keV line of ^{241}Am (a; 3 ns bin width) and the 122.1 keV line of ^{57}Co (b; 8 ns bin width). For each source, data was collected with the source illuminating the GeD from the LV face (orange, peaked at $\tau_{\text{CTD}} \sim -160 \text{ ns}$) and HV face (blue, peaked at $\tau_{\text{CTD}} \sim 180 \text{ ns}$).

For each event passing the selection criteria, τ_{CTD} was calculated as the difference between the calibrated TAC values on the HV strip and the LV strip. Fig. 2 presents the resulting τ_{CTD} distributions for an example pixel for both sources and both source positions. For the line energies in Tab. 2, λ_z is smaller than the GeD width. Thus, the τ_{CTD} distributions peak near the edges, corresponding to energy depositions near the illuminated face. At 59.5 keV, the events are entirely concentrated near the illuminated face, while at 122.1 keV, the entire detector width is illuminated for both source positions.

3. Simulation of Collection Time Difference

3.1. Collection Time Difference to Depth Mapping

This section describes the solid state detector and pulse shaping simulations that were used to create a mapping between τ_{CTD} and interaction depth z .

A GeD with the geometry and operating parameters summarized in Tab. 1 and material characteristics given in Tab. 3 was simulated using the Julia language-based **SolidStateDetectors.jl** simulations package [30]. The coordinates were defined with the GeD centered on $(x, y, z) = (0, 0, 0)$ and aligned with the edge of LV (HV) strip 63 at $x = +37.1 \text{ mm}$ ($y = +37.1 \text{ mm}$) and the HV face at $z = +7.6 \text{ mm}$. The electric potential and electric field

Table 3: Parameters in the `SolidStateDetectors.jl` simulation.

Ionization energy	2.95 eV
Fano factor	0.129
Density	5.323 g cm ⁻³
Dielectric constant	16.0 ϵ_0
Electron diffusion coefficient	239 cm ² s ⁻¹
Hole diffusion coefficient	279 cm ² s ⁻¹
Initial charge cloud radius	20 μ m
Longitudinal effective electron mass	1.64 m _e
Transverse effective electron mass	0.0819 m _e

were numerically computed throughout the sensitive volume, and the weighting potential was computed for each contact.

Fig. 3 illustrates the simulated GeD and ASIC response to a single energy deposition. Electron and hole clouds corresponding to a 59.5 keV energy deposition were generated with $(x, y, z) = (+0.58 \text{ mm}, +0.58 \text{ mm}, +4.60 \text{ mm})$, centered within the area of a sample pixel and 3.0 mm from the HV contact. The propagation of the electrons and holes was simulated in the `SolidStateDetectors.jl` framework, including diffusion and self-repulsion effects. A charge carrier drift velocity model with a powerlaw temperature dependence was used, with electron and hole mobility defined following Ref. [34]. The charge induced on the contacts was recorded as a function of time, with 1 ns sampling. To produce the semi-Gaussian pulses in Fig. 3, waveforms from the `SolidStateDetectors.jl` simulation were processed through a 5-channel SPICE-based⁵ [35] simulation of the ASIC electronics, and the simulated fast-shaper output was plotted for the channels of interest.

In Fig. 3, the signal on the HV strip rises \sim 120 ns before the signal on the LV strip. This is because the charge cloud was generated 3.0 mm (12.2 mm) from the HV (LV) face, so in this example the holes traverse a longer distance to the LV contact than the electrons to the HV contact. The vertical lines indicate the time τ_p of the peak of the fast shaper. In the ASIC, the TAC clock starts at τ_p , and the TAC value for that channel is its clock time at the end of the event. τ_{CTD} is defined as:

$$\tau_{\text{CTD}} := \text{TAC}_{\text{HV}} - \text{TAC}_{\text{LV}} = \tau_{p,\text{LV}} - \tau_{p,\text{HV}}. \quad (2)$$

For the example in Fig. 3, the signal on the HV strip rises before the LV strip, $\text{TAC}_{\text{HV}} > \text{TAC}_{\text{LV}}$, and $\tau_{\text{CTD}} > 0$.

Fig. 4 illustrates the relationship between τ_{CTD} and z . Charge clouds were injected at 0.05 mm increments across the 15.2 mm thick GeD. For each charge injection, the waveforms were simulated and processed as in Fig. 3. The resulting curve shows an approximately linear relation across much of the crystal width, with a steepening

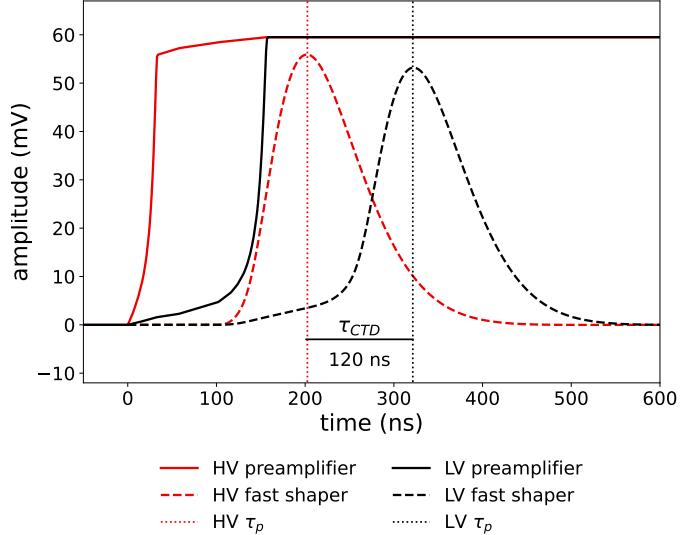


Figure 3: Simulated waveforms on the HV (red) and LV (black) contacts resulting from a charge cloud generated at $z = +4.6 \text{ mm}$ in the detector and centered laterally on the example pixel. For both contacts, simulated pulses are illustrated after processing through the preamplifier (solid) and fast shaper (dashed). The dotted vertical lines indicate τ_p , the start time for the TAC clocks at the peak of the shaped signal. τ_{CTD} is calculated according to Eq. (2) at 120 ns.

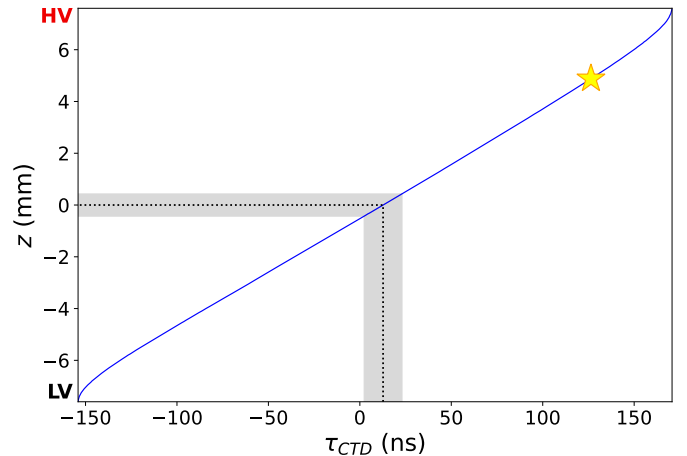


Figure 4: The simulated relation between charge collection time difference (τ_{CTD} ; defined in Eq. (2)) and interaction depth (z) is illustrated in blue. The HV face is at $z = +7.6 \text{ mm}$. The waveform illustrated in Fig. 3 constitutes a single point (indicated by the star) on this curve. The depth resolution (Δz) is calculated at depth z by mapping z to τ_{CTD} (black dotted line), adding the τ_{CTD} resolution (gray band) and mapping the band back onto depth.

(increased $\delta z / \delta \tau_{\text{CTD}}$) near the faces of the GeD due to the sharp weighting field arising from the small-pixel effect as well as charge induced by electrons (holes) on the hole-collecting (electron-collecting) contacts.

3.2. Simulated τ_{CTD} Distributions

In this section, the exponential distribution of interaction depths discussed in Sec. 2.2, the $\tau_{\text{CTD}}-z$ map calculated in Sec. 3.1, and a Gaussian timing resolution are

⁵<https://ptolemy.berkeley.edu/projects/embedded/pubs/downloads/spice/index.htm>

combined to simulate a τ_{CTD} distribution for a given energy and source position.

The ideal τ_{CTD} distribution was modeled for the λ_z^c values in [Tab. 2](#) and the two source positions by defining 1000 bins spanning the simulated τ_{CTD} range, mapping the respective exponential depth distribution into those bins, convolving with a Gaussian timing resolution σ_{CTD} , and linearly interpolating between the points using the `interp1d` functionality from SciPy [\[36\]](#). The result is a τ_{CTD} probability density function (PDF) that depends on the effective attenuation coefficient λ_z and the timing resolution σ_{CTD} .

4. Per-pixel Depth Calibration

In this section, the τ_{CTD} distributions for each individual pixel from [Sec. 2.2](#) were fitted with a PDF generated as in [Sec. 3.2](#) to validate the simulated $\tau_{\text{CTD}}\text{-}z$ map and to extract the timing resolution and thus the uncertainty on a depth reconstruction.

First, to facilitate fitting of data from the nearly 4000 pixels in the GeD, cumulative density functions (CDFs) were generated spanning $2 \text{ ns} < \sigma_{\text{CTD}} < 30 \text{ ns}$ with 0.05 ns step size for each λ_z and illuminated face. The CDF as a continuous function of σ_{CTD} was defined by interpolating between the pre-calculated curves.

For each pixel and for each source with its characteristic line energy, a binned negative log-likelihood cost function was defined simultaneously relating the HV- and LV-illuminated data to the respective model. For each fit, an offset and a stretch parameter were defined such that

$$\tau_{\text{CTD,data}} = (\tau_{\text{CTD,sim}} + \text{offset}) \cdot \text{stretch}. \quad (3)$$

Varying stretch and offset in the fit allows for variations in material properties or crystal width across the lateral extent of the GeD [\[18\]](#), as well as errors on the charge mobility parameters in the charge-drift model. While stretch and offset were common between the HV- and LV-illuminated data, σ_{CTD} varied independently for the two distributions, for a total of four free parameters. To avoid biasing the fit, bins with fewer than 5 counts were masked prior to minimization. The cost function was reduced using the `migrad` fitting routine from `iMinuit` [\[37\]](#), and errors were evaluated using `minos`.

[Fig. 5](#) illustrates the τ_{CTD} data and best fit simulated curve for both sources, for the example pixel from [Fig. 2](#). Overall, the ability of the simulated τ_{CTD} distributions to fit the data validates the use of the simulated $\tau_{\text{CTD}}\text{-}z$ mapping for depth calibration in this GeD. The best fit stretch and offset are consistent between the fits at the two energies. The 8% stretch factor indicates that the real charge drift times are 8% longer than predicted in simulation, compared to an $\sim 10\%$ error on the simulated charge drift mobility values reported in several works [\[30, 38, 39\]](#). The $\sim 3 \text{ ns}$ offset could indicate mismodeling of the relative drift velocity for electrons vs holes but is also less than the

reported 5.5 ns uncertainty in the TAC calibration offset for this pixel and thus can also be entirely explained by calibration error. The fitted stretch and offset are further discussed in [Sec. 5](#) in the context of the full GeD.

The reported $\Delta\tau_{\text{CTD}}$ is the full-width at half maximum timing resolution, calculated as $2.355 \cdot \sigma_{\text{CTD}} \cdot \text{stretch}$. The best-fit $\Delta\tau_{\text{CTD}}$ values are inconsistent between the HV- and LV-illuminated data at 59.5 keV. This could indicate that assumptions of the model — such as the assumption of constant $\Delta\tau_{\text{CTD}}$ over the depth of the GeD — may be incorrect, or that the fit is being distorted by variable correlations. Because the 59.5 keV photons travel only short distances into the GeD, the τ_{CTD} distributions at 59.5 keV pick up effects within $\sim 1 - 2 \text{ mm}$ of the faces, while the 122.1 keV distributions both probe the entire thickness. Comparison of the result at 59.5 keV and 122.1 keV indicates an energy-dependence of the timing resolution, which is finer at higher energies.

[Fig. 6](#) illustrates the depth resolution (Δz ; FWHM) as a function of interaction depth for the example pixel fitted in [Fig. 5](#). As illustrated in [Fig. 4](#), $\Delta z(z)$ was calculated by mapping z to τ_{CTD} , finding the τ_{CTD} range corresponding to $\Delta\tau_{\text{CTD}}$, and mapping the range of τ_{CTD} values back into z , accounting for stretch and offset in comparison with the simulated map. This mapping was performed using the mean of the HV- and LV-best-fit $\Delta\tau_{\text{CTD}}$ values at 59.5 keV and 122.1 keV. The finer $\Delta\tau_{\text{CTD}}$ at the higher-energy line corresponds to a finer Δz . Over most of the detector's thickness, Δz is nearly independent of z . However, Δz increases near the contacts, where small changes in τ_{CTD} result in large changes in reconstructed z . The gray curves indicate the value of Δz if z is allowed to be reconstructed at any value of z . The sharp peaks occur as an artifact when energy depositions are constrained to reconstruction within the thickness of the GeD.

5. Full Detector Depth Calibration

The fitting procedure in [Sec. 4](#) was performed for every pixel. This section discusses results for the GeD overall. Of the 3984 pixels, the 64 pixels of LV strip 14 were excluded due to anomalous behavior of the ASIC channel. Additionally, one pixel was excluded from the ^{241}Am data and ten pixels were excluded from the ^{57}Co data because the fits failed to converge.

[Fig. 7](#) illustrates Δz (FWHM) at $z = 0 \text{ mm}$ for the HP52301-1 pixels for the ^{241}Am line at 59.5 keV and the ^{57}Co line at 122.1 keV. As demonstrated in [Fig. 6](#), Δz at $z = 0 \text{ mm}$ is representative of Δz over most of the width. At 59.5 keV (122.1 keV), the average pixel has $\Delta z = 0.82 \text{ mm}$ ($\Delta z = 0.52 \text{ mm}$). [Fig. 7](#) indicates a significant energy dependence in Δz . Finer $\Delta\tau_{\text{CTD}}$, and thus finer Δz , is anticipated at higher energies, where the signal-to-noise ratio on the fast shaper is more favorable. Full modeling of the energy dependence is deferred to a future study.

At a given energy, $\Delta\tau_{\text{CTD}}$ for the HV- and LV-illuminated τ_{CTD} distributions are systematically

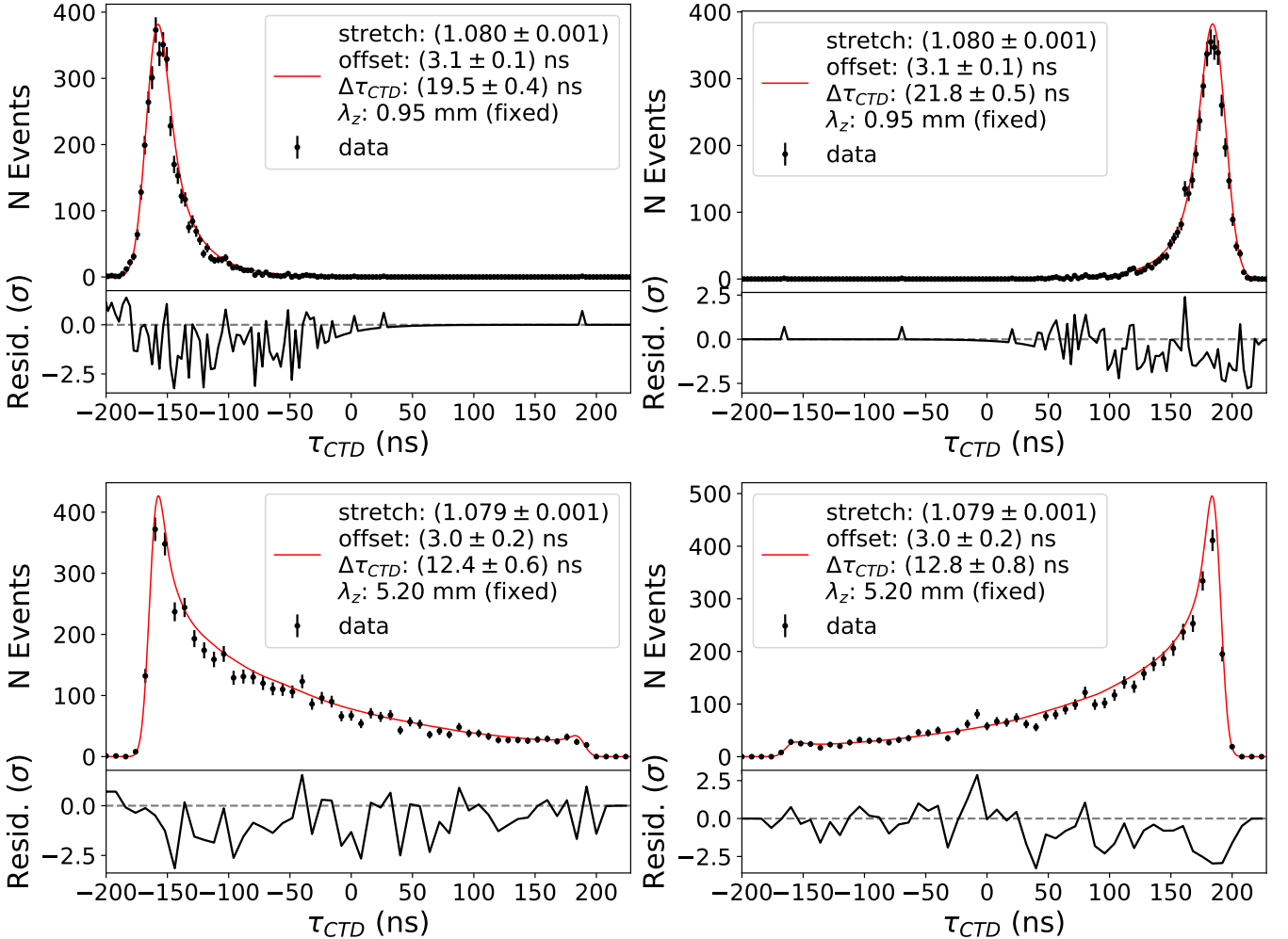


Figure 5: Fitted τ_{CTD} distributions for a single pixel illuminated with ^{241}Am (upper) and ^{57}Co (lower) from the LV (left) and HV (right) faces. The ^{57}Co and ^{241}Am fits were performed independently, but resulted in consistent fitted values for the stretch and offset. For each source, distributions from the two source positions were fitted jointly, with only $\Delta\tau_{CTD}$ allowed to vary between the LV- and HV-illuminated data. Residuals are reported based on the most probable number of counts in a bin according to the model.

different and linearly correlated. The trend is most stark for ^{241}Am , where the regression $\Delta\tau_{CTD,LV} = 0.9 \cdot \Delta\tau_{CTD,HV} + 0.6$ ns gives $\sigma = 0.3$ ns on the residuals. The effect is less significant for ^{57}Co , possibly because the entire GeD thickness is illuminated with both source positions at 122.1 keV or because of the lower quality of the fits overall. Though the difference between $\Delta\tau_{CTD}$ on the HV vs the LV face is a $\sim 10\%$ effect, small compared to the overall $\Delta\tau_{CTD}$, this result indicates that the assumption of constant $\Delta\tau_{CTD}$ for a pixel at a given energy does not necessarily hold, and motivates a deeper future investigation into the position dependence of $\Delta\tau_{CTD}$.

Fig. 8 illustrates the fitted stretch and offset from ^{241}Am and ^{57}Co , mapped across the lateral extent of the GeD. A slight energy dependence in the stretch was observed, as the mean percent stretch over all of the pixels was 1.073 (1.068) at 59.5 keV (122.1 keV) with pixel-to-pixel variation $\sigma_{\text{stretch}} = 0.009$ at both energies. If this effect is real, its impact on the reconstructed z is

a < 1 ns effect at $\tau_{CTD} = 180$ ns, much less than $\Delta\tau_{CTD}$, but it still motivates further study at higher energies. At either energy, the result is somewhat smaller than the expected $\sim 10\%$ error in the charge mobility model [30, 38, 39]. Error in the measured GeD thickness, in the extrapolated temperature, or in the TAC calibration could contribute to this deviation, though these contributions are expected to be at the sub-percent level. A population of pixels in LV strip 0 with anomalously long drift times (larger stretch) may indicate a local defect in the crystal structure or an impact of the guard ring electrode or nearby Al holder on the electric fields. Overall, the charge drift time is greater for the central pixels and decreases at larger radii, except for the very edge pixels. This suggests lateral inhomogeneities in physical characteristics such as the impurity concentration or crystal thickness, or edge effects on the electric field. The longer drift times in the edge pixels are more likely related to non-uniform electric fields near edges of the crystal or near the larger guard

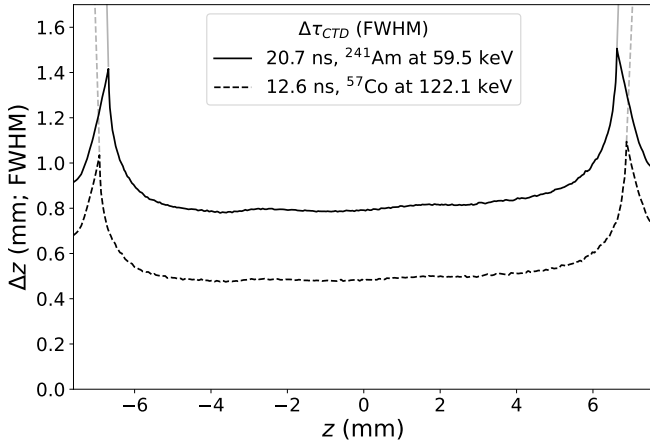


Figure 6: Depth resolution (Δz ; FWHM) as a function of interaction depth (z), for the mean $\Delta\tau_{CTD}$ obtained for the pixel in Fig. 5 at 59.5 keV (solid) and 122.1 keV (dashed). For this pixel, $\Delta z = 0.79$ mm (0.48 mm) at $z = 0$ mm for $\Delta\tau_{CTD} = 20.7$ ns (12.6 ns). For 70% of the GeD thickness, $-5.8 \text{ mm} < z < 4.9 \text{ mm}$, Δz is within 10% of the $z = 0$ mm level.

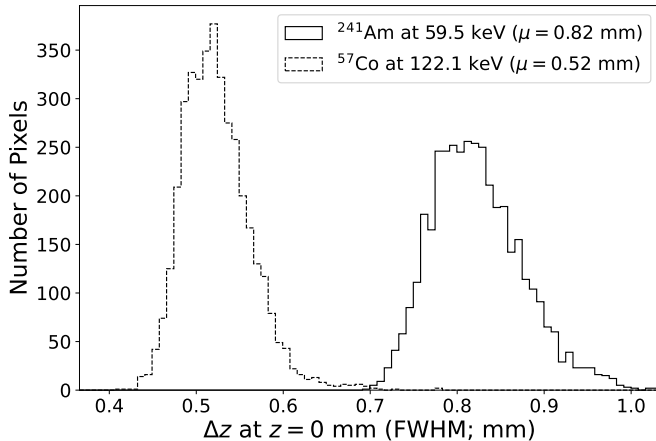


Figure 7: Δz (FWHM; $z = 0$ mm) for all pixels with converging fits. The calculation was based on the mean of the HV- and LV-fitted $\Delta\tau_{CTD}$ at each energy.

ring contacts.

For both energies, the mean offset is 0 ns, with an 11 ns standard deviation over the pixel population. The offsets are also very strongly correlated between the two fits for a given pixel. This indicates that the drift velocity model is correctly reproducing the relative difference in the electron and hole drift times, but some other factor is responsible for the pixel-to-pixel variation. The reported uncertainty in the TAC calibration per strip indicates an expected 8 ns standard deviation in the τ_{CTD} offsets based only on TAC calibration uncertainties. Examination of the strip-by-strip trends in Fig. 8 supports the hypothesis that most of the fitted offset for a typical pixel can be described as the combination of a calibration ‘offset’ from each of its constituent strips.

6. Conclusion

The ability to precisely reconstruct the 3D position of energy depositions in detectors is critical for Compton event reconstruction and thus for Compton imaging. Development of this capability in double-sided strip GeDs has enabled MeV imaging capability with a compact Compton telescope design. In the COSI GeDs, position in x and y is primarily determined by associating energy depositions with an orthogonal pair of 1.162 mm-wide strips. The depth z of interaction is extrapolated from the relative arrival time of charge at either face.

This work departs from previous depth calibration of similar GeDs both in terms of the hardware and in terms of the methods. The GeD in this work differs from those in previous work in the number of strips and in the strip pitch. Additionally, this is the first demonstration of the depth calibration using the COSI satellite-model ASIC readout. This work also represents the first depth calibration for a double-sided cross-strip GeD with τ_{CTD} - z mapping based on the `SolidStateDetectors.jl` simulation package, which was validated for timing simulations in the COSI GeDs based on compatibility with measured τ_{CTD} distributions.

The depth resolution has been reported for two low-energy γ -ray lines, 59.5 keV and 122.1 keV. This is in contrast to previous work, which used a continuum spectrum from the scattering of 661.7 keV photons from ^{137}Cs [18]. The use of two distinct lines highlights the energy dependence of the timing resolution, and by extension the depth resolution, in this energy range.

This study motivates several deeper investigations into the timing characteristics of the COSI GeDs, including characterization of:

- the energy- and depth-dependence of the timing resolution;
- the impacts of dead layers, impurity gradients in z , and other effects that could affect electric fields near the contacts;
- the impacts of lateral impurity gradients and thickness-nonuniformity on the drift velocity characteristics across the GeD; and
- edge effects, guard ring effects, and other factors that could impact electric fields near the edge of the GeD.

Additionally, this work selected events for which the line energy was primarily contained within a single strip. The depth calibration method for the case of charge sharing between adjacent strips requires treatment of the systematic timing effects of moving charges on neighboring strips. This study has been deferred to a future work. Finally, validation of the method using a few pixels illuminated by a fan beam is in progress and will also be reported in a future publication.

This work has demonstrated a method for calibrating the third positional dimension in the COSI satellite GeDs. Timing data from the ASIC has been mapped onto the depth of interaction, with a unique mapping and fitted depth resolution for each pixel. 90% of the pixels had depth resolution <0.9 mm at 59.5 keV and <0.6 mm at 122.1 keV at the center of the GeD's thickness. The calibration results from this GeD motivate detailed characterization of the timing characteristics of the COSI GeDs and ASICs.

Acknowledgment

The Compton Spectrometer and Imager is a NASA Explorer project led by the University of California, Berkeley with funding from NASA under contract 80GSFC21C0059.

We gratefully acknowledge the effort by the developers of the `SolidStateDetectors.jl` simulation framework, which has made this work possible. We also thank the members of the COSI collaboration's instrument and data pipeline teams for many enlightening discussions. F.R. thanks Martha E. Field for proofreading the manuscript.

Software: `SolidStateDetectors.jl` [30], MEGAlib [33], SPICE [35], Geant4 [28], iMinuit [37], Matplotlib [40], SciPy [36], NumPy [41], Pandas [42, 43].

References

- [1] Kroeger, R. A. *et al.* Spatial resolution and imaging of gamma rays with germanium strip detectors. In Siegmund, O. H. & Vallerga, J. V. (eds.) *EUV, X-Ray, and Gamma-Ray Instrumentation for Astronomy VI*, vol. 2518 of *Society of Photo-Optical Instrumentation Engineers (SPIE) Conference Series*, 236–243 (1995).
- [2] Amman, M. & Luke, P. Three-dimensional position sensing and field shaping in orthogonal-strip germanium gamma-ray detectors. *Nuclear Instruments and Methods in Physics Research A* **452**, 155–166 (2000).
- [3] Coburn, W. *et al.* 3D positioning germanium detectors for gamma-ray astronomy. In James, R. B. *et al.* (eds.) *X-Ray and Gamma-Ray Detectors and Applications IV*, vol. 4784, 54 – 63. International Society for Optics and Photonics (SPIE, 2003).
- [4] Amrose, S., Boggs, S., Coburn, W., Lin, R. & Smith, D. Calibration of 3d positioning in a ge cross-strip detector. *Nuclear Instruments and Methods in Physics Research A* **505**, 170–173 (2003). Proceedings of the tenth Symposium on Radiation Measurements and Applications.
- [5] Phlips, B. *et al.* Development and performance of large fine-pitch germanium strip detectors. In *IEEE Symposium Conference Record Nuclear Science 2004.*, vol. 4, 2110–2114 Vol. 4 (2004).
- [6] Bandstra, M. E. *et al.* Position calibrations and preliminary angular resolution of the prototype nuclear compton telescope. In *2006 IEEE Nuclear Science Symposium Conference Record*, vol. 2, 770–777 (2006).
- [7] Amman, M., Luke, P. & Boggs, S. Amorphous-semiconductor-contact germanium-based detectors for gamma-ray imaging and spectroscopy. *Nuclear Instruments and Methods in Physics Research A* **579**, 886–890 (2007). Proceedings of the 6th "Hiroshima" Symposium on the Development and Application of Semiconductor Detectors.
- [8] Amman, M. Optimization of Amorphous Germanium Electrical Contacts and Surface Coatings on High Purity Germanium Radiation Detectors (2018). arXiv:[1809.03046](https://arxiv.org/abs/1809.03046).
- [9] Sleator, C. C. *et al.* Benchmarking simulations of the Compton Spectrometer and Imager with calibrations. *Nuclear Instruments and Methods in Physics Research A* **946**, 162643 (2019). arXiv:[1911.02992](https://arxiv.org/abs/1911.02992).
- [10] Amman, M. High Purity Germanium Based Radiation Detectors with Segmented Amorphous Semiconductor Electrical Contacts: Fabrication Procedures (2020). arXiv:[2006.05471](https://arxiv.org/abs/2006.05471).
- [11] Duncan, N. *et al.* First flight of the Gamma-Ray Imager/Polarimeter for Solar flares (GRIPS) instrument. In den Herder, J.-W. A., Takahashi, T. & Bautz, M. (eds.) *Space Telescopes and Instrumentation 2016: Ultraviolet to Gamma Ray*, vol. 9905, 99052Q. International Society for Optics and Photonics (SPIE, 2016).
- [12] Boggs, S. E. *et al.* Overview of the nuclear Compton telescope. *New Astronomy Reviews* **48**, 251–255 (2004).
- [13] Bandstra, M. S. *et al.* Detection and Imaging of the Crab Nebula with the Nuclear Compton Telescope. *Astrophysical Journal* **738**, 8 (2011). arXiv:[1106.0323](https://arxiv.org/abs/1106.0323).
- [14] Kierans, C. *et al.* The 2016 Super Pressure Balloon flight of the Compton Spectrometer and Imager. In *11th INTEGRAL Conference Gamma-Ray Astrophysics in Multi-Wavelength Perspective*, 75 (2016).
- [15] Tomsick, J. *et al.* The Compton Spectrometer and Imager. In *Bulletin of the American Astronomical Society*, vol. 51, 98 (2019). arXiv:[1908.04334](https://arxiv.org/abs/1908.04334).
- [16] Tomsick, J. & COSI Collaboration. The Compton Spectrometer and Imager Project for MeV Astronomy. In *37th International Cosmic Ray Conference*, 652 (2022). arXiv:[2109.10403](https://arxiv.org/abs/2109.10403).

[17] Tomsick, J. A. *et al.* The Compton Spectrometer and Imager. In *Proceedings of 38th International Cosmic Ray Conference — PoS(ICRC2023)*, vol. 444, 745 (2023). arXiv:2308.12362.

[18] Lowell, A. *et al.* Positional calibrations of the germanium double-sided strip detectors for the Compton spectrometer and imager. In Holland, A. D. & Beletic, J. (eds.) *High Energy, Optical, and Infrared Detectors for Astronomy VII*, vol. 9915, 99152H. International Society for Optics and Photonics (SPIE, 2016).

[19] He, Z. Review of the shockley–ramo theorem and its application in semiconductor gamma-ray detectors. *Nuclear Instruments and Methods in Physics Research A* **463**, 250–267 (2001).

[20] Barrett, H. H., Eskin, J. D. & Barber, H. B. Charge transport in arrays of semiconductor gamma-ray detectors. *Physical Review Letters* **75**, 156–159 (1995).

[21] Liu, Z.-K. *et al.* Characterizing and Correcting the Cross-Talk Effect on Depth Measurement in the NCT Detectors. *IEEE Transactions on Nuclear Science* **56**, 1210–1214 (2009).

[22] Beechert, J. *et al.* Calibrations of the Compton Spectrometer and Imager. *Nuclear Instruments and Methods in Physics Research A* **1031**, 166510 (2022). arXiv:2203.00695.

[23] Pike, S. N. *et al.* Characterizing and correcting electron and hole trapping in germanium cross-strip detectors. *Nuclear Instruments and Methods in Physics Research A* **1056**, 168562 (2023). arXiv:2306.08778.

[24] Boggs, S. E. & Pike, S. N. Analytical fitting of γ -ray photopeaks in germanium cross strip detectors. *Experimental Astronomy* **56**, 403–420 (2023). arXiv:2305.01544.

[25] Boggs, S. E. Modeling charge cloud dynamics in cross strip semiconductor detectors. *Nuclear Instruments and Methods in Physics Research A* **1052**, 168310 (2023). arXiv:2304.09713.

[26] Boggs, S. E. *et al.* Numerical simulations of charge trapping in germanium strip detectors. *Nuclear Instruments and Methods in Physics Research A* **1057**, 168756 (2023). arXiv:2310.01312.

[27] Pike, S. N. *et al.* Characterizing hole trap production due to proton irradiation in germanium cross-strip detectors. *Experimental Astronomy* **59**, 8 (2025). arXiv:2412.08836.

[28] Agostinelli, S. *et al.* Geant4—a simulation toolkit. *Nuclear Instruments and Methods in Physics Research A* **506**, 250–303 (2003).

[29] Bezanson, J., Edelman, A., Karpinski, S. & Shah, V. B. Julia: A fresh approach to numerical computing. *SIAM Review* **59**, 65–98 (2017).

[30] Abt, I. *et al.* Simulation of semiconductor detectors in 3d with solidstatedetectors.jl. *Journal of Instrumentation* **16**, P08007 (2021).

[31] Wulf, E. A. *et al.* Front-end ASIC for germanium strip detectors. *Nuclear Instruments and Methods in Physics Research A* **954**, 161230 (2020).

[32] Berger, M. *et al.* Xcom: Photon cross section database (version 1.5) (2010). [Online] <https://physics.nist.gov/PhysRefData/Xcom/html/xcom1.html>, National Institute of Standards and Technology, Gaithersburg, MD.

[33] Zoglauer, A., Andritschke, R. & Schopper, F. MEGAlib The Medium Energy Gamma-ray Astronomy Library. *New Astronomy Reviews* **50**, 629–632 (2006).

[34] Bruyneel, B., Reiter, P. & Pascovici, G. Characterization of large volume hpge detectors. part i: Electron and hole mobility parameterization. *Nuclear Instruments and Methods in Physics Research A* **569**, 764–773 (2006).

[35] Nagel, L. W. & Pederson, D. Spice (simulation program with integrated circuit emphasis). Tech. Rep. UCB/ERL M382 (1973). URL <http://www2.eecs.berkeley.edu/Pubs/TechRpts/1973/22871.html>.

[36] Virtanen, P. *et al.* SciPy 1.0: Fundamental Algorithms for Scientific Computing in Python. *Nature Methods* **17**, 261–272 (2020).

[37] Dembinski, H. *et al.* scikit-hep/iminuit (2024). URL <https://doi.org/10.5281/zenodo.13902219>.

[38] Caughey, D. & Thomas, R. Carrier mobilities in silicon empirically related to doping and field. *Proceedings of the IEEE* **55**, 2192–2193 (1967).

[39] Mihailescu, L., Gast, W., Lieder, R., Brands, H. & Jäger, H. The influence of anisotropic electron drift velocity on the signal shapes of closed-end hpge detectors. *Nuclear Instruments and Methods in Physics Research A* **447**, 350–360 (2000).

[40] Hunter, J. D. Matplotlib: A 2d graphics environment. *Computing in Science & Engineering* **9**, 90–95 (2007).

[41] Harris, C. R. *et al.* Array programming with NumPy. *Nature* **585**, 357–362 (2020).

[42] McKinney, W. Data structures for statistical computing in python. In *Proceedings of the 9th Python in Science Conference*, vol. 445, 51–56 (Austin, TX, 2010).

[43] pandas development team, T. pandas-dev/pandas: Pandas (2020). URL <https://doi.org/10.5281/zenodo.3509134>.

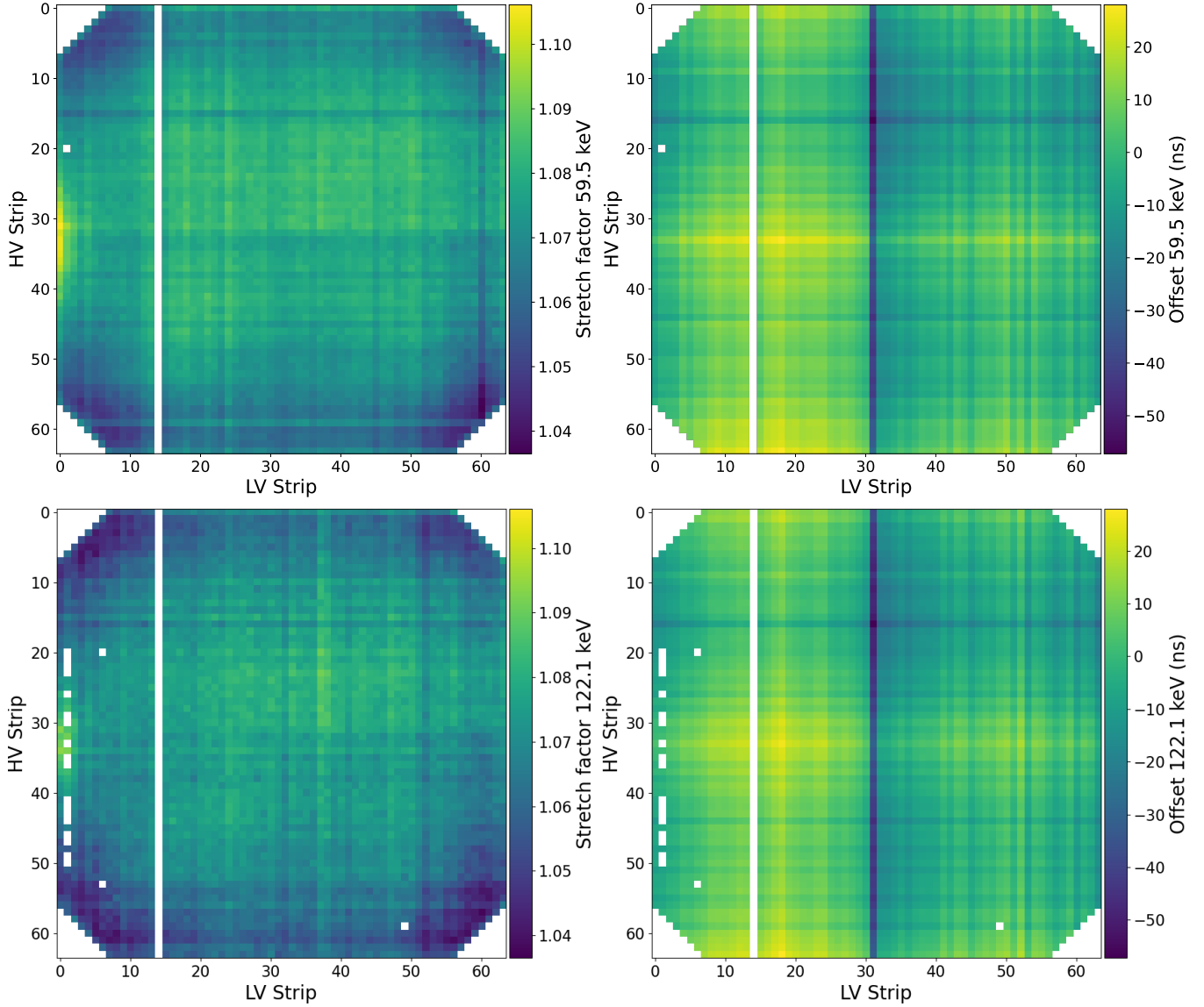


Figure 8: Pixel map of the best-fit stretch (left) and offset (right) from Eq. (3) in ^{241}Am (upper) and ^{57}Co (lower). As illustrated in Fig. 1, the 7 strips nearest each edge have fewer than 64 pixels per strip in order to fit into the crystal geometry, resulting in the missing corner pixels. At both energies, the stretch factor varies by $<10\%$ across the GeD. A radially-dependent pattern is apparent, where the stretch factor is higher (longer drift times) toward the center of the detector and smaller at larger radii, except that the edge pixels feature anomalously high stretch. By contrast, the offset values appear primarily determined by the HV and LV strips rather than a spatial pattern over the detector surface, indicating that the variation primarily originates in the TAC calibration, which is performed on a per-strip basis.